# Continuous BaTi1–yZryO3 (0≤y≤1) nanocrystals synthesis in supercritical fluids for nanostructured lead-free ferroelectric ceramics

Gilles Philippot, Marjorie Albino, U-Chan Chung, Michaël Josse, Catherine Elissalde, Mario Maglione, Cyril Aymonier

# Continuous $BaTi_{1-y}Zr_yO_3$ ($0 \leq y \leq 1$) nanocrystals synthesis in supercritical fluids for nanostructured lead-free ferroelectric ceramics

Gilles Philippot[1] , Marjorie Albino[1] , U-Chan Chung[1], Michaël Josse[1], Catherine Elissalde[1] , Mario Maglione[1] , Cyril Aymonier[1]

[1] *Univ. Bordeaux, CNRS, Bordeaux INP, ICMCB, UMR 5026, F-33600 Pessac, France*

**Abstract :** This paper addresses for the first time two of the main challenges in the field of electroceramics. The first one is the development of a continuous, fast and reliable synthesis method for producing sub-20 nm barium titanate zirconate (BaTi1-yZryO3 with $0 \leq y \leq 1$–BTZ) nanocrystals over the whole solid solution, while keeping a narrow size distribution. The second one concerns the processing of dense and nanostructured lead free electroceramics highlighting the size effect on the crossover from ferroelectric to relaxor, in the case of grains smaller than 100 nm. This was achieved combining the supercritical fluid technology to produce in continuous and at moderate temperature (400 °C) BTZ nanocrystals, with Spark Plasma Sintering (SPS) to prevent grain growth during the sintering.

**Keywords :** Barium titanate zirconate (BTZ), Supercritical fluid, Nanocrystal, Nanostructured ceramic, Lead free, Ferroelectric, Relaxor

## 1. Introduction

The versatility of barium titanate zirconate ($BaTi_{1-y}Zr_yO_3$ with $0 \leq y \leq 1$–BTZ) intrinsic properties by adjusting the zirconium/titanium ratio makes this material attractive for basic and applied researches. The sharp ferroelectric to paraelectric phase transition for $y \leq 0.15$ becomes broader increasing the substitution rate from 0.15 up to 0.25. A further increase up to 0.40 leads to a relaxor behaviour characterized by a frequency dependent dielectric permittivity maximum [1–7]. Such a material with a ferroelectric-relaxor crossover, exhibiting thus tunable dielectric behaviour, presents a high potential in terms of applications. It can be used as multilayer capacitor ceramic (MLCC), lead-free piezoelectric transducers, chemical sensors, microwave devices and so on.

Currently, one of the most suitable routes for synthesizing BTZ materials is the solid state one. However, due to zirconium precursor reactivity, such route requires very high temperatures (up to 1200 °C) to obtain chemically homogeneous BTZ powders. Still, this method encounters limitations for producing the $BaZrO_3$-rich region of the solid solution [8–10]. In this context, alternative methods have been developed such as the chemical solution deposition [4,11], the hydrothermal [12–14], the direct synthesis from solution [15], or the sonochemical one [16], but the synthesis in the $BaZrO_3$-rich region remains a challenge. Among these methods only the one based on a modified vapour diffusion sol–gel process, is reported as enabling the synthesis of BTZ nanocrystals over the entire solid solution [6,17–19]. This process, involving the stirring of Ba–Zr and Ba–Ti double metal alkoxide solution (less than 1 mmol) under a $N_2$ bubbled HCl gas flow for 72 h, is time consuming and limits the production to tiny amount of material with a yield estimated around 70 to 80%. Moreover, in this case, the nanoparticles processing into ceramics was not investigated.

All together, these aspects make the reliable screening of BTZ ceramics over the whole solid solution challenging. To solve this issue we propose to use the supercritical fluid process together with Spark Plasma Sintering (SPS) [20]. This synthesis technology, besides being scalable, enables the single step and reliable synthesis of a wide range of highly crystalline nanoparticles in a very short time (few seconds), at moderate pressure (≤250 bar) and temperature (≤400 °C) [21–27]. This technology can be thus considered as the best option for a large scale production of high quality BTZ nanocrystals. Moreover, combining such advanced synthesis route with fast ceramic processing technology enables to achieve high density ceramics while keeping nanoscale grain size. It becomes then possible to probe the grain size dependence of lead free ferroelectric ceramics. In literature, such effect on the relaxor behaviour is mainly reported in lead based compounds. Regarding the lead free nanostructured ceramics, this was mainly discussed in the BCTZ

* Corresponding author at: CNRS, ICMCB, UPR 9048, F-33600 Pessac, France.
*E-mail address:* cyril.aymonier@icmcb.cnrs.fr (C. Aymonier).

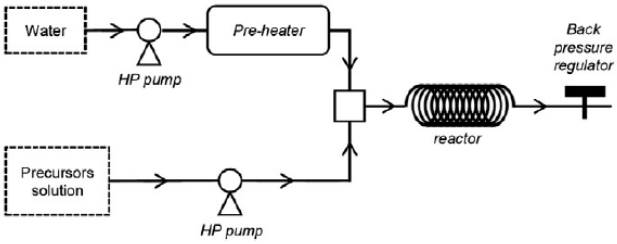


**Fig. 1.** Supercritical flow setup used for producing BTZ nanocrystals.

case [28–31]. Such lack in the materials property understanding must be filled out to develop the nanosized components required for a higher degree of integration in electronic devices.

To the best of our knowledge, we report in this study both: i) the first fast and continuous synthesis of BTZ nanocrystals over the entire solid solution, from $BaTiO_3$ to $BaZrO_3$ using supercritical fluid synthesis and ii) the first processing of lead free BTZ nanostructured ceramics (sub-100 nm grains) by SPS along with their microstructural and dielectric characterizations.

## 2. Experimental

### 2.1. Supercritical fluid synthesis of BTZ nanocrystals

#### 2.1.1. Materials

Barium, titanium and zirconium isopropoxides (99.9% trace metals basis) and ethanol (≥99.8%) were purchased from Sigma-Aldrich. The precursors are weighted following a barium to titanium molar ratio of 1 and the concentration of the $Ba^{2+}$, $Ti^{4+}$ or $Zr^{4+}$ ions in anhydrous ethanol can be varied at will. However, taking into account the processability, an optimized concentration in barium and titanium of $3.10^{-2}$ mol·L$^{-1}$ was chosen. The solution is stirred in a hermetically closed bottle for at least 30 min prior to the injection.

#### 2.1.2. Method

The setup used was already described elsewhere [32]. It is made of two injection lines, one for the precursor solubilized in ethanol and the other for water (Fig. 1). The water line was preheated at 150 °C before being mixed with the precursor solution to speed up the heating rate inside the reactor. However the precursor line was kept at room temperature to avoid side reactions. The temperature and pressure within the 24 m tubular reactor of 1/8 in. were set at 400 °C and 23 MPa, respectively. The flow rate of both injection lines was 6 g·min$^{-1}$ enabling to have a turbulent flow (Reynolds number - Re> 3000) with a ratio of ethanol to water ($x_{ethanol}$) of 0.29 and a residence time estimated around 50 s. Such mixture presents a critical point at $T_C$ = 305 °C and 13 ≤ $P_C$ ≤ 17 MPa, which is lower than the one of pure water (Tc = 374 °C and Pc = 22.1 MPa) [33]. It is important to note that based on these flow rates, the concentration in precursor inside the reactor drops to approximately $1.3 \cdot 10^{-2}$ mol·L$^{-1}$.

With these experimental conditions the BTZ nanocrystals were synthesized at the gram scale with a molar yield above 90%.

### 2.2. Powder characterizations

#### 2.2.1. X-ray diffraction

Diffraction patterns were recorded at room temperature with a PANalytical X'Pert MPD-PRO powder diffractometer equipped with a germanium monochromator to be perfectly monochromatic. We observed only the diffraction of the Cu K$\alpha_1$ radiation at $\lambda_1$ = 1.54060 Å generated at 45 kV and 40 mA.

These XRD patterns were refined using the FullProf software and the Thompson–Cox–Hastings formulation of the pseudo-Voigt function was applied to describe the peak profiles [34]. The following parameters were refined: the instrumental zero point, the scale factor, the unit cell parameters, the Gaussian and Lorentzian size broadening contributions and the global Debye–Waller-factors.

The crystallite sizes (<D>) were calculated with the Scherrer Eq. (1) based on the Gaussian ($I_G$) and Lorentzian (Y) contributions to the total size broadening defined in Eq. (2) λ is the wavelength and K was set at 0.94 for this study [35–37].

$$\langle D \rangle = \frac{K \cdot \lambda}{H \cdot \cos(\theta)} \tag{1}$$

$$\begin{aligned} H = (&\sqrt{I_G}^{5} + 2.69269 \cdot \sqrt{I_G}^{4} \cdot Y \\ &+2.48243 \cdot \sqrt{I_G}^{3} \cdot Y^2 \\ &+ 4.47163 \cdot \sqrt{I_G}^{2} \cdot Y^3 \\ &+0.07842 \cdot \sqrt{I_G} \cdot Y^4 + Y^5)^{1/5}. \end{aligned} \tag{2}$$

The uncertainties ($\sigma_D$) were calculated with Eqs. (3) & (4) where $\sigma_{IG}$ and $\sigma_Y$ are the uncertainties on $I_G$ and Y determined through the refinements. In all the results the errors on size calculations were below the nanometre showing both: data and samples of high quality.

$$\sigma_D = \left(\frac{0.94\lambda}{H^2}\right) \cdot \sigma_H \tag{3}$$

$$\sigma_H = \frac{\pi}{180} \cdot \sqrt{\frac{Y}{16\, {I_G}^{2/3}} \cdot {\sigma_{I_G}}^2 + \frac{\sigma_{I_G}}{4Y} \cdot {\sigma_Y}^2}. \tag{4}$$

#### 2.2.2. Transmission electron microscopy (TEM)

Two different apparatus were used:

- A HITACHI H7650 (owned by the Bordeaux Imaging Center) with an accelerating voltage from 80 to 120 kV which can operate in high contrast or high resolution. Such apparatus enables to have a resolution of 1 nm according to the nature of the material analysed. In our case, we worked in high resolution mode where the magnification can reach ×600,000. The detector is an ORIUS SC1000 11MPx (GATAN) camera and we used the Digital Micrograph (GATAN) software to acquire the images.

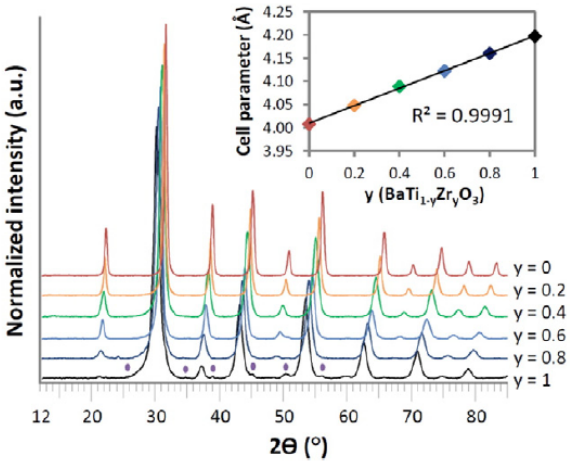


**Fig. 2.** Powder XRD patterns of the synthesized BTZ (0 ≤ y ≤ 1) solid solution (note a BaO + $ZrO_2$ contamination (•) for the $BaZrO_3$ powder) together with the variation of the BTZ (0 ≤ y ≤ 1) lattice parameter *a* according to y, the zirconium molar content.

**Table 1**
Main parameters obtained from the BTZ powder XRD pattern refinements.

| Parameters | Compositions | | | | | |
|---|---|---|---|---|---|---|
| | $BaTiO_3$ | $BaTi_{0.8}Zr_{0.2}O_3$ | $BaTi_{0.6}Zr_{0.4}O_3$ | $BaTi_{0.4}Zr_{0.6}O_3$ | $BaTi_{0.2}Zr_{0.8}O_3$ | $BaZrO_3$ |
| Space group | P4mm | Pm3m | Pm3m | Pm3m | Pm3m | Pm3m |
| Cell parameter (Å) | a = 4.0080 | a = 4.0481 | a = 4.0892 | a = 4.1223 | a = 4.1602 | a = 4.1969 |
| | b = 4.0080 | b = 4.0481 | b = 4.0892 | b = 4.1223 | b = 4.1602 | b = 4.1969 |
| | c = 4.0236 | c = 4.0481 | c = 4.0892 | c = 4.1223 | c = 4.1602 | c = 4.1969 |
| Scale factor | $1.0243 \cdot 10^{-2}$ | $6.2262 \cdot 10^{-2}$ | $2.3436 \cdot 10^{-2}$ | $5.9645 \cdot 10^{-2}$ | $5.3228 \cdot 10^{-2}$ | $4.5634 \cdot 10^{-2}$ |
| Y(Lorentzian contribution) | 0.22708 | 0.35965 | 0.37783 | 0.45098 | 0.72736 | 1.05916 |
| $\sigma_Y$ | 0.00281 | 0.00207 | 0.00350 | 0.00453 | 0.00408 | 0.00541 |
| $I_{G\ (Gaussian\ contribution)}$ | 0.08715 | 0.04797 | 0.14860 | 0.14217 | 0.19089 | 0.00329 |
| $\sigma_{IG}$ | 0.00096 | 0.00080 | 0.00165 | 0.00219 | 0.00250 | 0.00035 |
| Bragg R-factor | 2.39 | 2.29 | 3.8 | 2.58 | 1.16 | 1.50 |
| Rf-factor | 0.849 | 2.39 | 2.33 | 1.98 | 0.961 | 1.08 |
| Chi2 | 2.71 | 7.75 | 3.22 | 8.79 | 2.65 | 3.34 |

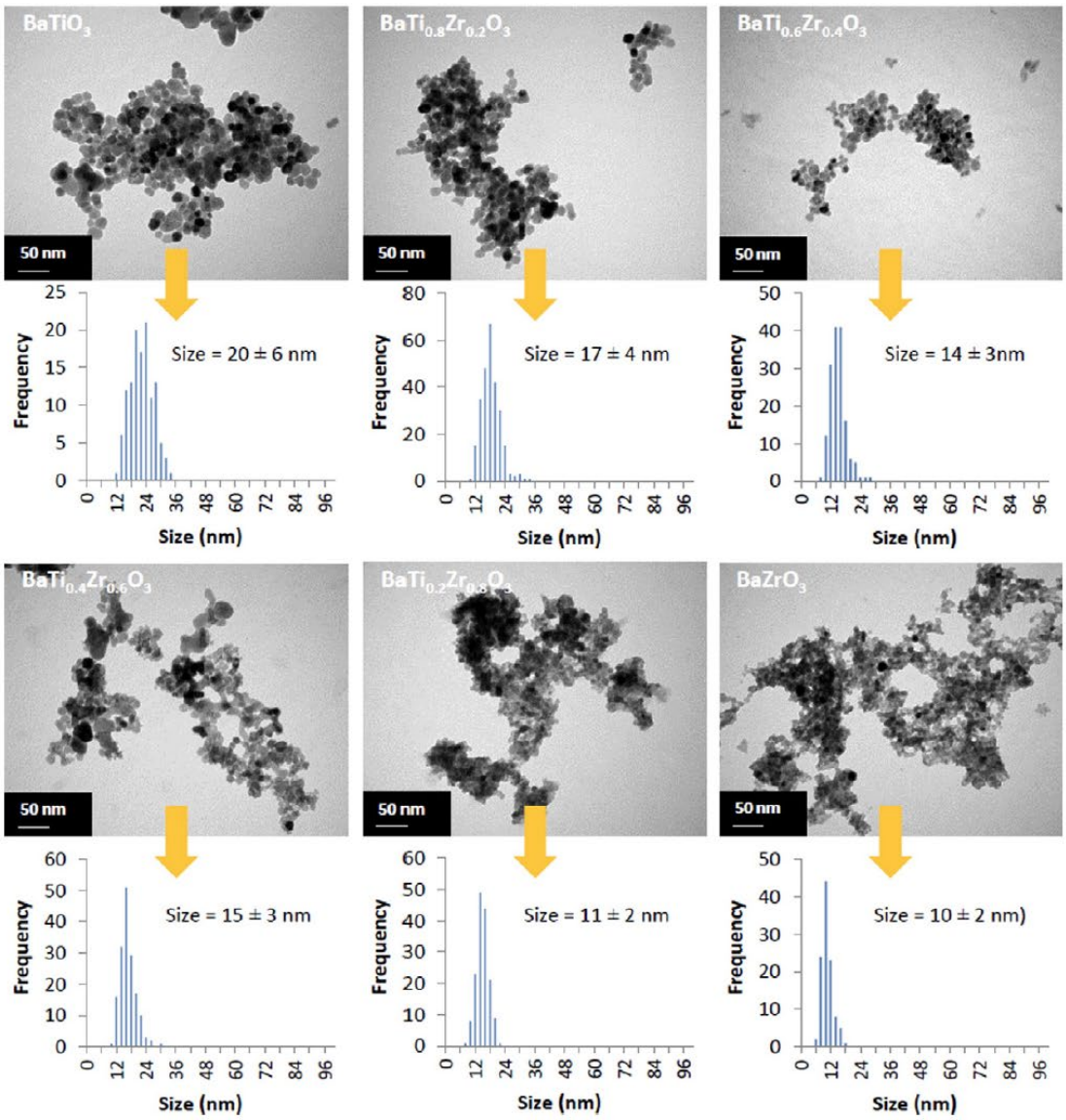


**Fig. 3.** TEM images of the BTZ nanocrystals produced along the entire solid solution together with their size distributions determined with more than 150 nanocrystals for each composition.

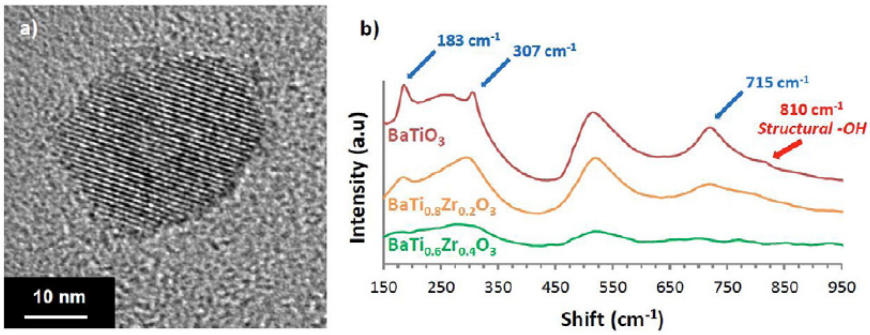


**Fig. 4.** $BaTi_{0.8}Zr_{0.2}TiO_3$ powder characterization: (a) High resolution TEM image and (b) Raman spectra at room temperature for y = 0, 0.2 and 0.4.

- A JEOL 2200FS with an accelerating voltage of 200 kV and equipped with a high resolution camera. In this case, the resolution is 0.23 nm. Again, the Digital Micrograph (GATAN) software was used to acquire the images.

*2.2.3. Raman spectroscopy*

The Raman spectrometer used a DXR dispersive microscope with a 532 nm wavelength excitation laser operating at 8 mW output power. The focus is made with a confocal microscope with a ×10 objective, leading to a surface analysis of 3.5 $\mu m^2$. The resolution was 3 $cm^{-1}$ over a window from 15 to 3550 $cm^{-1}$.

*2.3. Nanostructured BTZ ceramics: processing and characterization*

*2.3.1. Spark plasma sintering (SPS)*

In comparison to the conventional sintering process, for which the main limitation for nanopowder consolidation is the duration of the thermal cycle, SPS enables very high heating rates and short dwell times of few minutes, leading to enhanced sintering kinetics. Using this technique it is possible to obtain dense materials keeping the initial grain size of the nanoparticles. A Dr. Sinter 515S machine manufactured by the society SPS Syntex Inc. was used. This apparatus has an output pulsed current of 1500 A, a voltage ranging from 2 to 20 V and can apply a pressure up to 200 MPa. The sintering temperature was set at 1200 °C (heating rate of 100 °C·$min^{-1}$) for 3 min applying a uniaxial pressure of 90 MPa. Prior to any characterization, the ceramics were annealed 10 h at 1000 °C to avoid detrimental conductivity arising from $Ti^{4+}$ reduction into $Ti^{3+}$ during the SPS step performed under low oxygen partial pressure [38–42].

*2.3.2. Scanning electron microscopy (SEM)*

To characterize the grain sizes of the ceramics SPS processed, a high resolution SEM, a JEOL JSM 6700F with an accelerating voltage from 0.5 to 30 kV and magnification up to 650,000, was used.

*2.3.3. Dielectric measurements*

The measurements were carried out with an automatic HP 4194 impedance bench developed at Institut de Chimie et de la Matière Condensée de Bordeaux from the Centre National de la Recherche Scientifique (ICMCB–CNRS) in a frequency range from 100 Hz to 1 MHz. Gold electrodes were deposited on two parallel faces of the ceramic and the real and imaginary contributions of the permittivity, ε′ and ε″, were respectively determined from the measured values of capacitance (C) and losses (tan δ) from Eqs. (5) and (6):

$$\varepsilon' = \frac{C \cdot e}{\varepsilon_0 \cdot S} \quad (5)$$

$$\tan \delta = \frac{\varepsilon''}{\varepsilon'} \quad (6)$$

where $\varepsilon_0$ is the vacuum permittivity ($\varepsilon_0 = 8.854187 \cdot 10^{-12}$ F·$m^{-1}$), S is the surface of the electrodes (in $m^2$), e the thickness of the dielectric material (in m). The contribution from the measurement apparatus is removed through its calibration in open and short circuits.

## 3. Results and discussion

To demonstrate our statement, BTZ nanoparticles with y = 0; 0.2; 0.4; 0.5; 0.6; 0.8 and 1 were produced to properly screen the entire solid solution. Fig. 2 presents the X-ray diffraction (XRD) patterns of the synthesized nanoparticles normalized to the most intense peak.

As expected, increasing the zirconium content induces a regular shift of the diffraction peaks towards lower angles. According to literature, at room temperature bulk $BaTiO_3$ exhibits a tetragonal structure, which becomes pseudo-cubic from y > 0.05 and then cubic for y > 0.15 [5,6]. In the present study, the lattice parameters were determined describing $BaTiO_3$ with the P4mm space group and all the other compositions with the Pm-3 m one (see Table 1 for a summary of the refined parameters). The lattice parameter *a* is thus considered when comparing the different compositions. Fig. 2 also shows a linear variation of the BTZ lattice parameter *a* according to the zirconium content (y). Such an evolution, in good agreement with the empirical Vegard's law, enables to confirm the synthesis of the entire solid solution.

Fig. 3 presents the TEM images for all the BTZ powders produced in supercritical fluid conditions together with the histograms of the particles sizes determined with more than 150 particles for each composition. A decrease in both particles size and size distribution is observed with an increase of zirconium atoms. Indeed, the average particle size decreases from 20 ± 6 nm, for $BaTiO_3$, down to 15 ± 3 nm when increasing the zirconium content up to $BaTi_{0.4}Zr_{0.6}TiO_3$ and finally reaches 10 ± 2 nm for $BaZrO_3$ nanoparticles. A similar trend was observed in Philippot et al. study of the $Ba_xSr_{1-x}TiO_3$ (with $0 \le x \le 1$) solid solution obtained in similar conditions [32].

Focusing on $BaTi_{0.8}Zr_{0.2}O_3$ composition, the high resolution TEM image in Fig. 4a supports the synthesis process quality through the appearance of lattice fringes along the entire particle. To confirm the production of nanocrystals, the crystallite size was calculated with the Scherrer equation, using the Gaussian and Lorentzian contributions

**Table 2**
Comparison between BTZ crystallites (from XRD) and particles sizes (from TEM).

| Composition | Crystallites size from XRD (nm) | Particles size from TEM (nm) |
|---|---|---|
| $BaTiO_3$ | 19 | 20 ± 6 |
| $BaTi_{0.8}Zr_{0.2}O_3$ | 18 | 17 ± 4 |
| $BaTi_{0.6}Zr_{0.4}O_3$ | 13 | 14 ± 3 |
| $BaTi_{0.4}Zr_{0.6}O_3$ | 12 | 15 ± 3 |
| $BaTi_{0.2}Zr_{0.8}O_3$ | 9 | 11 ± 2 |
| $BaZrO_3$ | 8 | 10 ± 2 |

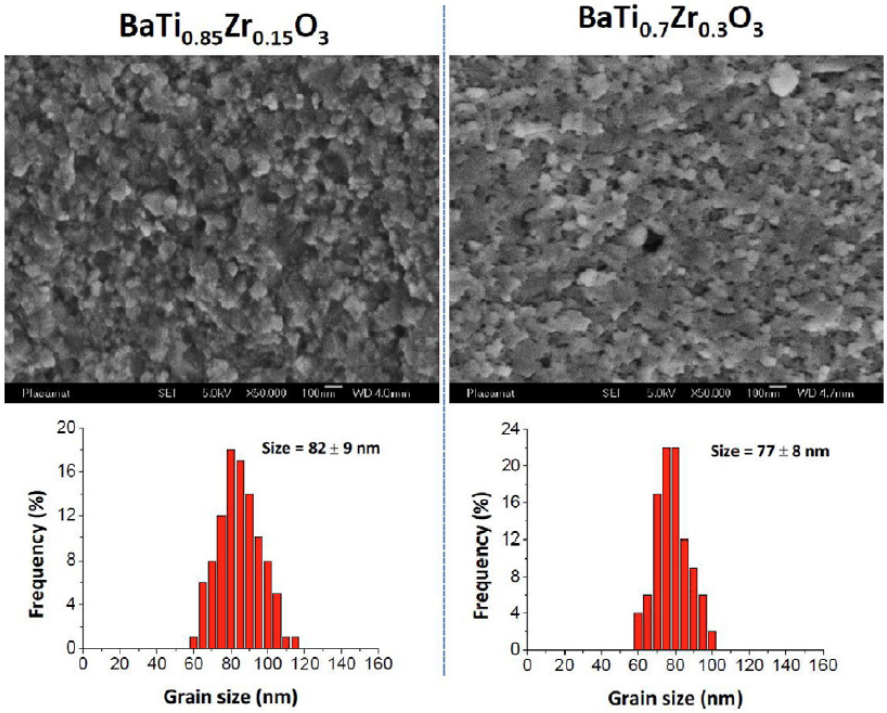


**Fig. 5.** SEM images of $BaTi_{0.85}Zr_{0.15}O_3$ and $BaTi_{0.70}Zr_{0.30}O_3$ ceramics after annealing with their measured grain size distribution (measured over 100 grains in each case).

(determined with the refinements) to the total size broadening. A particle size of 18 nm (uncertainties below 1 nm) was obtained, in good agreement with the 17 ± 4 nm obtained from TEM image (Fig. 3).

The result in the case of $BaTi_{0.8}Zr_{0.2}O_3$ composition was extended to the entire solid solution and the comparison between the particle sizes measured from TEM images and the crystallite sizes calculated (Table 2) confirmed the synthesis of nanocrystals along the entire BTZ solid solution.

The Raman spectrum of $BaTi_{0.8}Zr_{0.2}O_3$ (Fig. 4b), exhibiting active modes at 183 $cm^{-1}$ associated with those at 307 $cm^{-1}$ and 715 $cm^{-1}$, supports the presence of a long-range ferroelectric order on the B site within the perovskite structure remaining from the initial $BaTiO_3$ one. As expected, this long range order disappears for $BaTi_{0.6}Zr_{0.4}O_3$ which becomes cubic at room temperature [43–47]. This result supports the accuracy in terms of composition control of the supercritical fluid technology for BTZ synthesis. In addition, the structural –OH defects

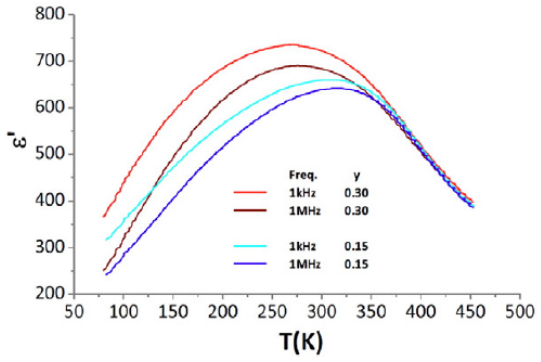


**Fig. 6.** Temperature dependence of the permittivity at 1 kHz and 1 MHz for $BaTi_{0.85}Zr_{0.15}O_3$ (in blue) and $BaTi_{0.7}Zr_{0.3}O_3$ (in red) ceramics.

observed are characteristic of wet syntheses and can impact the material properties [48].

To fully demonstrate the high level of control over the synthesis of the entire BTZ solid solution, two other compositions were prepared: $BaTi_{0.85}Zr_{0.15}TiO_3$ and $BaTi_{0.7}Zr_{0.3}TiO_3$ and confirmed by inductively coupled plasma (ICP) measurements. As presented in the Introduction, the first composition should behave as a classical ferroelectric while the second one is generally reported as a relaxor. Starting from these two nanopowders, ceramics were elaborated using SPS. Dense pellets (≈95% of relative density) were obtained with a significant reduction of both sintering temperature and duration compared to BTZ conventionally sintered ceramics (i.e. 1400–1500 °C during several hours). In addition, a control of the nanostructure was achieved as shown on high resolution images where the average grain size is estimated below 100 nm (Fig. 5).

Dielectric measurements on nanostructured ceramics were acquired in the frequency range of 100 Hz up to 1 MHz and in a temperature window of 70 up to 450 K (Fig. 6). Compared to bulk ceramics with micrometre grain size, the dielectric transition temperatures are observed in the expected temperature range according to the compositions i.e. 325 K (y = 0.15) and 270 K (y = 0.3). In the vicinity of room temperature, the permittivity values for these nano-scale ceramics are close to 700 instead of 3000 for micro-scale ones. Such a decrease in permittivity is fully consistent with a nanostructured ceramic.

However these permittivities remain higher than those reported by Rabuffetti et al., since in the later case only room temperature permittivity values of pressed compacts have been reported ($\varepsilon_r$ in the range 10–70 according to the composition) [5,6,14,43,47,49–51]. This is in good agreement with the high density of the obtained nanostructured ceramics. The two compositions exhibit diffuse dielectric phase transitions associated with a frequency dispersion whereas in bulk ceramics this is the case only for the composition y = 0.3. Indeed a classical ferroelectric behaviour (sharp maximum of permittivity independent of frequency) is well known in micro-sized BTZ solid solution until y = 0.15. The ferroelectric-relaxor crossover observed in bulk ceramics

when zirconium content reaches 0.15 could be shifted to a smaller Zr content due to size effect. Nevertheless, the amplitude of the dispersion ($\Delta\varepsilon'$1 kHz–1 MHz) is unambiguously higher for the composition y = 0.3 (6% and 2.7% for y = 0.3 and y = 0.15, respectively) and this dispersion vanishes well above the temperature of the maximum of permittivity for y = 0.3 whereas it disappears more abruptly and at a temperature closer to the transition for y = 0.15. These features support an evolution of the properties towards a relaxor behaviour when increasing Zr content. Finally, the superposition of dielectric responses (1 kHz–1 MHz) in the paraelectric region reflects the limitated amount of extrinsic defects at the grain boundaries and highlights the quality of our nanostructured ceramics despite the high density of grain boundaries.

## 4. Conclusion

Combining the supercritical chemistry route with Spark Plasma Sintering, we were able to: i) overcome the precursor reactivity encountered with conventional route and ii) strongly improve the sintering kinetics to enable the processing of ceramics in the entire BTZ system. The supercritical synthesis opens thus the challenging field of fundamental research focused on the study of size effect in lead free ceramics. However, in the framework of the present study, it would be necessary to consider the dynamics, the size and the concentration of nanopolar regions in order to investigate more deeply the relaxor behaviour in nanosized BTZ. Future works and experiments at very low temperature will be performed to complete the discussion on these aspects.

To summarize, i) the linear lattice parameter variation with increasing zirconium content, ii) the dielectric transition temperatures evolving as expected according to the composition iii) the evolution of the dielectric properties towards a relaxor behaviour when increasing Zr content, confirm the accuracy of the synthesis in terms of composition control. In addition, the entire BTZ solid solution can be accurately produced, the as obtained particles are monocrystalline (nanocrystals) and high quality nanostructured lead free ceramics can be prepared by SPS. The supercritical fluid synthesis can therefore be considered as an efficient and fast technological alternative towards metal oxide nanoparticle production such as BTZ. In combination with SPS, this synthesis route opens a new pathway towards the investigation of size effects in nanostructured lead free relaxor ceramics.

## Acknowledgements

The authors acknowledge the IDS FunMat European Doctoral School, the Region Aquitaine and the Agence Nationale de la Recherche (project ARCHIFUN -12-BS08-009) for their financial support. They also acknowledge the Bordeaux Imaging Center for their TEM facilities.

## References

[1] I.-K. Jeong, C.Y. Park, J.S. Ahn, S. Park, D.J. Kim, Ferroelectric-relaxor crossover in $BaTi_{1-x}Zr_xO_3$ studied using neutron total scattering measurements and reverse Monte Carlo modeling, Phys. Rev. B 81 (2010) 214119, http://dx.doi.org/10.1103/PhysRevB.81.214119.

[2] C. Kajtoch, Influence of Zr-substitution on phase transitions character in polycrystalline $Ba(Ti_{1-x}Zr_x)O_3$, J. Mater. Sci. 46 (2010) 1469–1473, http://dx.doi.org/10.1007/s10853-010-4948-8.

[3] J. Bera, S.K. Rout, On the formation mechanism of $BaTiO_3$–$BaZrO_3$ solid solution through solid-oxide reaction, Mater. Lett. 59 (2005) 135–138, http://dx.doi.org/10.1016/j.matlet.2004.07.053.

[4] J.F. Ihlefeld, J.-P. Maria, W. Borland, Dielectric and microstructural properties of barium titanate zirconate thin films on copper substrates, J. Mater. Res. 20 (2011) 2838–2844, http://dx.doi.org/10.1557/JMR.2005.0342.

[5] S. Miao, J. Pokorny, U.M. Pasha, O.P. Thakur, D.C. Sinclair, I.M. Reaney, Polar order and diffuse scatter in $Ba(Ti_{1-x}Zr_x)O_3$ ceramics, J. Appl. Phys. 106 (2009) 114111, http://dx.doi.org/10.1063/1.3253735.

[6] F.A. Rabuffetti, R.L. Brutchey, Local structural distortion of $BaZr_{(x)}Ti_{(1-x)}O_3$ nanocrystals synthesized at room temperature, Chem. Commun. (Camb.) 48 (2012) 1437–1439, http://dx.doi.org/10.1039/c1cc14166j.

[7] T. Maiti, R. Guo, A.S. Bhalla, Evaluation of experimental resume of $BaZr_xTi_{1-x}O_3$ with perspective to ferroelectric relaxor family: an overview, Ferroelectrics 425 (2011) 4–26, http://dx.doi.org/10.1080/00150193.2011.644168.

[8] T. Maiti, E. Alberta, R. Guo, A.S. Bhalla, The polar cluster like behavior in $Ti^{4+}$ substituted $BaZrO_3$ ceramics, Mater. Lett. 60 (2006) 3861–3865, http://dx.doi.org/10.1016/j.matlet.2006.03.130.

[9] T. Maiti, R. Guo, A.S. Bhalla, The evolution of relaxor behavior in $Ti^{4+}$ doped $BaZrO_3$ ceramics, J. Appl. Phys. 100 (2006) 114109, http://dx.doi.org/10.1063/1.2392996.

[10] D. Nuzhnyy, J. Petzelt, M. Savinov, T. Ostapchuk, V. Bovtun, M. Kempa, et al., Broadband dielectric response of Ba(Zr, Ti)O3 ceramics: from incipient via relaxor and diffuse up to classical ferroelectric behavior, Phys. Rev. B 86 (2012) 014106, http://dx.doi.org/10.1103/PhysRevB.86.014106.

[11] S. Halder, T. Schneller, U. Böttger, R. Waser, Fabrication and electrical characterisation of Zr-substituted $BaTiO_3$ thin films, Appl. Phys. A 81 (2004) 25–29, http://dx.doi.org/10.1007/s00339-004-3096-x.

[12] T. Kawano, K. Hashimoto, A. Nishida, T. Tsuchiya, Preparation and electrical properties of $Ba(Ti_{1-x}Zr_x)O_3$ thin films by hydrothermal method, J. Ceram. Soc. Jpn. 110 (2002) 530–534.

[13] X. Wu, J. Chen, Z. Shi, H. Huang, L. Liu, J. Yu, et al., Hydrothermal synthesis and photoluminescence properties of $BaZr_{1-x}Ti_xO_3$ hollow nanospheres, Mater. Lett. 86 (2012) 21–24, http://dx.doi.org/10.1016/j.matlet.2012.07.035.

[14] Z. Sun, Y. Pu, Z. Dong, Y. Hu, X. Liu, P. Wang, Effect of $Zr^{4+}$ content on the $T_C$ range and dielectric and ferroelectric properties of $BaZr_xTi_{1-x}O_3$ ceramics prepared by microwave sintering, Ceram. Int. 40 (2014) 3589–3594, http://dx.doi.org/10.1016/j.ceramint.2013.09.069.

[15] J.Q. Qi, X.H. Wang, H. Zhang, H. Zou, Z.B. Wang, X.W. Qi, et al., Direct synthesis of barium zirconate titanate (BZT) nanoparticles at room temperature and sintering of their ceramics at low temperature, Ceram. Int. 40 (2014) 2747–2750, http://dx.doi.org/10.1016/j.ceramint.2013.10.045.

[16] S. Wirunchit, T. Charoonsuk, N. Vittayakorn, Facile sonochemical synthesis of near spherical barium zirconate titanate (BaZr 1 − y Ti y O 3; BZT); perovskite stability and formation mechanism, RSC Adv. 5 (2015) 38061–38074, http://dx.doi.org/10.1039/C5RA04267D.

[17] F.A. Rabuffetti, J.S. Lee, R.L. Brutchey, Vapor diffusion sol–gel synthesis of fluorescent perovskite oxide nanocrystals, Adv. Mater. 24 (2012) 1434–1438, http://dx.doi.org/10.1002/adma.201104645.

[18] F.A. Rabuffetti, R.L. Brutchey, Local structure of $Ba_{(1-x)}Sr_{(x)}TiO_3$ and $BaTi_{(1-y)}Zr_{(y)}O_3$ nanocrystals probed by X-ray absorption and X-ray total scattering, ACS Nano 7 (2013) 11435–11444, http://dx.doi.org/10.1021/nn405629e.

[19] F.A. Rabuffetti, R.L. Brutchey, Complex perovskite oxide nanocrystals: low-temperature synthesis and crystal structure, Dalton Trans. 43 (2014) 14499–14513, http://dx.doi.org/10.1039/c4dt01376j.

[20] C. Elissalde, U.-C. Chung, G. Philippot, J. Lesseur, R. Berthelot, D. Sallagoity, et al., Innovative architectures in ferroelectric multi-materials: chemistry, interfaces and strain, J. Adv. Dielectr. 1530001 (2015) http://dx.doi.org/10.1142/S2010135X15300017.

[21] T. Adschiri, Y. Hakuta, K. Arai, Hydrothermal synthesis of metal oxide fine particles at supercritical conditions, Ind. Eng. Chem. Res. 39 (2000) 4901–4907, http://dx.doi.org/10.1021/ie0003279.

[22] T. Adschiri, Y.-W. Lee, M. Goto, S. Takami, Green materials synthesis with supercritical water, Green Chem. 13 (2011) 1380–1390, http://dx.doi.org/10.1039/c1gc15158d.

[23] C. Aymonier, A. Loppinet-Serani, H. Reverón, Y. Garrabos, F. Cansell, Review of supercritical fluids in inorganic materials science, J. Supercrit. Fluids 38 (2006) 242–251, http://dx.doi.org/10.1016/j.supflu.2006.03.019.

[24] H. Hayashi, Y. Hakuta, Hydrothermal synthesis of metal oxide nanoparticles in supercritical water, Materials 3 (2010) 3794–3817, http://dx.doi.org/10.3390/ma3073794.

[25] G. Philippot, C. Elissalde, M. Maglione, C. Aymonier, Supercritical fluid technology: a reliable process for high quality $BaTiO_3$ based nanomaterials, Adv. Powder Technol. 25 (2014) 1415–1429, http://dx.doi.org/10.1016/j.apt.2014.02.016.

[26] R. Sui, P. Charpentier, Synthesis of metal oxide nanostructures by direct sol–gel chemistry in supercritical fluids, Chem. Rev. 112 (2012) 3057–3082.

[27] F. Cansell, C. Aymonier, Design of functional nanostructured materials using supercritical fluids, J. Supercrit. Fluids 47 (2009) 508–516, http://dx.doi.org/10.1016/j.supflu.2008.10.002.

[28] H. Amorín, J. Ricote, R. Jiménez, J. Holc, M. Kosec, M. Algueró, Submicron and nanostructured $0.8Pb(Mg_{1/3}Nb_{2/3})O_3$–$0.2PbTiO_3$ ceramics by hot pressing of nanocrystalline powders, Scr. Mater. 58 (2008) 755–758, http://dx.doi.org/10.1016/j.scriptamat.2007.12.015.

[29] R. Grigalaitis, M. Ivanov, J. Macutkevic, J. Banys, J. Carreaud, J.M. Kiat, et al., Size effects in a relaxor: further insights into PMN, J. Phys. Condens. Matter 26 (2014) 272201, http://dx.doi.org/10.1088/0953-8984/26/27/272201.

[30] R. Jiménez, H. Amorín, J. Ricote, J. Carreaud, J. Kiat, B. Dkhil, et al., Effect of grain size on the transition between ferroelectric and relaxor states in $0.8Pb(Mg_{1/3}Nb_{2/3})O_3$–$0.2PbTiO_3$ ceramics, Phys. Rev. B 78 (2008) 094103, http://dx.doi.org/10.1103/PhysRevB.78.094103.

[31] X.-G. Tang, H.L.-W. Chan, Effect of grain size on the electrical properties of (Ba, Ca)(Zr, Ti)O3 relaxor ferroelectric ceramics, J. Appl. Phys. 97 (2005) 034109, http://dx.doi.org/10.1063/1.1849817.

[32] G. Philippot, K.M.Ø. Jensen, M. Christensen, C. Elissalde, M. Maglione, B.B. Iversen, et al., Coupling in situ synchrotron radiation with ex situ spectroscopy characterizations to study the formation of $Ba_{1-x}Sr_xTiO_3$ nanoparticles in supercritical fluids, J. Supercrit. Fluids 87 (2014) 111–117, http://dx.doi.org/10.1016/j.supflu.2013.12.009.

[33] A.R. Bazaev, I.M. Abdulagatov, E.A. Bazaev, A. Abdurashidova, (p, v, T, x) Measurements of {(1 − x)H2O + xC2H5OH} mixtures in the near-critical and supercritical regions, J. Chem. Thermodyn. 39 (2007) 385–411, http://dx.doi.org/10.1016/j.jct.2006.08.002.

[34] P. Thompson, D.E. Cox, J.B. Hastings, Rietveld refinement of Debye–Scherrer synchrotron X-ray data from A1203, J. Appl. Phys. 20 (1987) 79–83.

[35] J.L. Langford, A.J.C. Wilson, Scherrer after sixty years: a survey and some new results in the determination of crystallite size, J. Appl. Crystallogr. 11 (1978) 102–113.

[36] B.E. Warren, X-ray Diffraction, 1990.
[37] A.C. Larson, R.B. Von Dreele, General Structure Analysis, System (GSAS), vol. 7482004.
[38] J.H. Noh, K.S. Hong, H.S. Jung, J.-K. Lee, Dielectric properties of nanocrystalline $TiO_2$ prepared using spark plasma sintering, J. Electroceram. 17 (2006) 913–917, http://dx.doi.org/10.1007/s10832-006-8574-4.
[39] J.H. Noh, H.S. Jung, J.-K. Lee, J.-R. Kim, K.S. Hong, Microwave dielectric properties of nanocrystalline $TiO_2$ prepared using spark plasma sintering, J. Eur. Ceram. Soc. 27 (2007) 2937–2940, http://dx.doi.org/10.1016/j.jeurceramsoc.2006.11.018.
[40] Z. Valdez-Nava, S. Guillemet-Fritsch, C. Tenailleau, T. Lebey, B. Durand, J.Y. Chane-Ching, Colossal dielectric permittivity of $BaTiO_3$-based nanocrystalline ceramics sintered by spark plasma sintering, J. Electroceram. 22 (2008) 238–244, http://dx.doi.org/10.1007/s10832-007-9396-8.
[41] Z. Valdez-Nava, C. Tenailleau, S. Guillemet-Fritsch, N. El Horr, T. Lebey, P. Dufour, et al., Structural characterization of dense reduced $BaTiO_3$ and $Ba_{0.95}La_{0.05}TiO_3$ nanoceramics showing colossal dielectric values, J. Phys. Chem. Solids 72 (2011) 17–23, http://dx.doi.org/10.1016/j.jpcs.2010.10.016.
[42] S. Yoon, J. Dornseiffer, Y. Xiong, D. Grüner, Z. Shen, S. Iwaya, et al., Spark plasma sintering of nanocrystalline $BaTiO_3$-powders: consolidation behavior and dielectric characteristics, J. Eur. Ceram. Soc. 31 (2011) 1723–1731, http://dx.doi.org/10.1016/j.jeurceramsoc.2011.03.035.
[43] R. Farhi, M. El Marssi, A. Simon, J. Ravez, A Raman and dielectric study of ferroelectric $Ba(Ti_{1-x}Zr_x)O_3$ ceramics, Eur. Phys. J. B 9 (1999) 599–604.
[44] N.K. Karan, R.S. Katiyar, T. Maiti, R. Guo, A.S. Bhalla, Raman spectral studies of $Zr^{4+}$ rich $BaZr_xTi_{1-x}O_3$ ($0.5 \le x \le 1.00$) phase diagram, J. Raman Spectrosc. 40 (2009) 370–375, http://dx.doi.org/10.1002/jrs.2134.
[45] M. El Marssi, Y. Gagou, J. Belhadi, F. De Guerville, Y.I. Yuzyuk, I.P. Raevski, Ferroelectric $BaTiO_3/BaZrO_3$ superlattices: X-ray diffraction, Raman spectroscopy, and polarization hysteresis loops, J. Appl. Phys. 108 (2010) 084104, http://dx.doi.org/10.1063/1.3496620.
[46] L.R. Macario, M.L. Moreira, J. Andrés, E. Longo, An efficient microwave-assisted hydrothermal synthesis of $BaZrO_3$ microcrystals: growth mechanism and photoluminescence emissions, CrystEngComm 12 (2010) 3612, http://dx.doi.org/10.1039/c004034g.
[47] M. Deluca, C.A. Vasilescu, A.C. Ianculescu, D.C. Berger, C.E. Ciomaga, L.P. Curecheriu, et al., Investigation of the composition-dependent properties of BaTi1 − xZrxO3 ceramics prepared by the modified Pechini method, J. Eur. Ceram. Soc. 32 (2012) 3551–3566, http://dx.doi.org/10.1016/j.jeurceramsoc.2012.05.007.
[48] M. Maglione, G. Philippot, D. Levasseur, S. Payan, C. Aymonier, C. Elissalde, Defect chemistry in ferroelectric perovskites: long standing issues and recent advances, Dalton Trans. (2015)http://dx.doi.org/10.1039/C5DT01897H.
[49] W. Kleemann, S. Miga, J. Dec, J. Zhai, Crossover from ferroelectric to relaxor and cluster glass in BaTi1 − xZrxO3 (x = 0.25–0.35) studied by non-linear permittivity, Appl. Phys. Lett. 102 (2013) 232907, http://dx.doi.org/10.1063/1.4811089.
[50] P.S. Dobal, A. Dixit, R.S. Katiyar, Z. Yu, R. Guo, A.S. Bhalla, Micro-Raman scattering and dielectric investigations of phase transition behavior in the $BaTiO_3$–$BaZrO_3$ system, J. Appl. Phys. 89 (2001) 8085, http://dx.doi.org/10.1063/1.1369399.
[51] A. Simon, J. Ravez, M. Maglione, The crossover from a ferroelectric to a relaxor state in lead-free solid solutions, J. Phys. Condens. Matter 16 (2004) 963–970, http://dx.doi.org/10.1088/0953-8984/16/6/023.